Statistical analysis of the turbulent Reynolds stress and its link to the shear flow generation in a cylindrical laboratory plasma device

Z. Yan, J. H. Yu, C. Holland, M. Xu, S. H. Müller, and G. R. Tynan
Center for Energy Research, University of California, San Diego, La Jolla, California 92093, USA

(Received 5 June 2008; accepted 25 August 2008; published online 24 September 2008)

The statistical properties of the turbulent Reynolds stress arising from collisional drift turbulence in a magnetized plasma column are studied and a physical picture of turbulent driven shear flow generation is discussed. The Reynolds stress peaks near the maximal density gradient region, and is governed by the turbulence amplitude and cross-phase between the turbulent radial and azimuthal velocity fields. The amplitude probability distribution function (PDF) of the turbulent Reynolds stress is non-Gaussian and positively skewed at the density gradient maximum. The turbulent ion-saturation (Isat) current PDF shows that the region where the bursty Isat events are born coincides with the positively skewed non-Gaussian Reynolds stress PDF, which suggests that the bursts of particle transport appear to be associated with bursts of momentum transport as well. At the shear layer the density fluctuation radial correlation length has a strong minimum ($\sim 4-6$ mm $\sim 0.5C_s/\Omega_{ci}$, where C_s is the ion acoustic speed and Ω_{ci} is the ion gyrofrequency), while the azimuthal turbulence correlation length is nearly constant across the shear layer. The results link the behavior of the Reynolds stress, its statistical properties, generation of bursty radially going azimuthal momentum transport events, and the formation of the large-scale shear layer.
 [DOI: 10.1063/1.2985836]

I. INTRODUCTION

In magnetic confinement fusion devices the anomalous transport across the magnetic field is thought to be caused by plasma turbulence. The two fundamental instabilities are thought to be the interchange instability and the drift wave instability.[1,2] Theory suggests for a given background pressure gradient, the turbulence saturation occurs via the formation of a large-scale shear flow that is generated by the turbulence Reynolds stress (radial transport of azimuthal momentum) which mediates the nonlinear transfer of turbulent momentum and kinetic energy into the larger scaled shear flow. The shear flows can also mitigate turbulence by tearing apart turbulent eddies, resulting in the formation of a self-regulating complex system.[3] Many experimental studies in tokamaks have provided evidence of the existence of shear flow during the transition from L mode to H mode,[4–6] as well as in stationary discharges.[7] In recent experiments carried out on the Controlled Shear Decorrelation eXperiment (CSDX) linear device, a radially sheared azimuthal flow has been demonstrated to be sustained by the Reynolds stress against ion-neutral collisional and viscous damping through the analysis of momentum balance, providing a direct experimental test of the theory of drift-turbulence/shear flow interaction.[8,9]

In all the theoretical and experimental studies of turbulence/shear flow interactions the Reynolds stress plays an important role. However, in the existing publications, only the measured mean Reynolds stress profile and its link with the large-scale shear flow have been examined;[6,10–12] to date there has been no study of how the turbulent statistical properties (e.g., turbulence amplitudes, cross-phases, cross-coherency) lead to the development of the detailed Reynolds stress profile associated with the shear flow. Furthermore, no detailed experimental study of the link between the turbulent Reynolds stress, background shear flow, and formation of bursty transport events has been carried out. In large-scale fusion devices direct measurement of the Reynolds stress with Langmuir probe is difficult because of the high plasma density and electron temperature. Laboratory-scale plasmas, in contrast, provide an opportunity to provide such detailed results.

This paper provides such a detailed study of the statistical properties of the turbulent Reynolds stress in a laboratory-scale plasma device and uses these results to build a physical picture of shear flow generation from turbulent momentum transport that is consistent with experimental observations. The results show that the cross-phase between turbulent radial and azimuthal velocity fields plays an important role in determining the divergence of the turbulent Reynolds stress, which drives or reinforces shear flow between the density gradient maximum and the peak shear layer (we denote this region as the negative viscosity region, since the turbulent shear stress is acting to reinforce the shear flow); at other radial locations the Reynolds stress dissipates shear flow. Bursts of outward-going positive density fluctuations are born at or near the density gradient maximum, and carry positive azimuthal momentum, resulting in a positive Reynolds stress in this region. As the fluctuations move outwards from the maximum density gradient and towards the shear layer their amplitudes decrease, resulting in a gradual decrease in the positive Reynolds stress, which then results in a negative stress divergence that reinforces the shear flow. These results indicate that a system of radially propagating turbulent structures which are immersed within a background seed shear flow naturally form a Reynolds stress profile that then acts to reinforce the shear flow.

We have also examined the role that the collisional ion-ion viscosity plays in determining the time-averaged azimuthal flow profile. Collisional viscosity acts to transfer azimuthal flow from the shear layer located at the periphery of the plasma column into the central plasma region. If this viscosity is strong enough then it will give (nearly) solid body azimuthal rotation near the plasma axis resulting in the formation of plasma rotation in the central region away from the shear layer. The similarities of these results with observations in tokamak devices are pointed out, suggesting that the observations may be a universal signature of turbulent-driven shear flows interacting with bursty transport events, and may also be related to recent reports of links between edge plasma flows and so-called "intrinsic rotation" in the core of tokamak plasmas.

The rest of the paper is organized as follows: In Sec. II we briefly describe our experimental setup. In Sec. III, we present our probe measurements of turbulent Reynolds stress, while in Sec. IV we show the statistical properties of the Reynolds stress. In Sec. V we compare with intermittent density fluctuations, following it are the Sec. VI discussions, and lastly in Sec. VII we review and summarize our results.

II. EXPERIMENTAL SETUP

The experiments presented here are carried out on a linear machine CSDX plasma device. This device is operated with a 13.56 MHz, 1500 W RF helicon wave source via an antenna surrounding a 10 cm diameter glass bell jar. A matching circuit is adjusted such that less than 30 W of power is reflected. The device has an overall length of 2.8 m and a diameter of 0.2 m. Both source and vacuum chamber are surrounded by a set of disk-shaped electromagnet coils, providing a solenoidal magnetic field that can be varied from 0 up to 1 kG. The typical working gas pressure is $P=3$ mTorr and a 1000 l/s turbopump is located downstream from the source. The typical peak plasma density is $\sim 10^{19}$ m^{-3}, electron temperature is ~ 3 eV, the ion temperature is $\sim 0.5-0.7$ eV, and the neutral gas temperature is $\leqslant 0.4$ eV. All of the magnetic field lines exiting the two ends of the device terminate on insulating surfaces to eliminate the possibility of currents flowing through the end plates of the device. Thus, any axial currents due to drift waves must be balanced by cross-field currents carried by ion polarization drifts (which are equivalent to the turbulent Reynolds stress[13]). A more detailed description of the machine can be found in the literature.[14,15]

Measurements of mean plasma profiles, the fluctuating density, potential, and electric fields along with the resulting turbulent Reynolds stress are made by an 18-tip Langmuir probe inserted radially in a port located 1.7 m downstream from the source. Same quantities are also measured in the upstream port located 1 m from the source, which show the same results indicating that axial gradients are weak and thus the dynamics are quasi-two-dimensional. The 18 tips are arranged as two 3×3 arrays, which are shifted with respect to each other along the B field direction by 1.5 mm. One 3×3 array measures floating potential and another one measures ion-saturation (Isat) current, biased by −25 V. Each tip is 0.33 mm in diameter and 1 mm in length. Each tip is in a single ceramic tube with diameter only 1.2 mm. Figures 1(a) and 1(b) show the schematic of the probe array. The arrangements of the probe tips allow the calculation of radial and azimuthal electric fields at the same position (φ_6 and φ_4 are used to calculate E_θ; φ_8 and φ_2 are used to calculate E_r), which thus give the Reynolds stress assuming that the plasma particles execute $E\times B$ drifts. Such arrangements also ensure that when calculating the cross-phase between the radial and the azimuthal velocity fields, there is no spurious phase shifts. The probe is manually moved in the radial direction in 2 mm increments to get a radial profile of the measuring quantities. A digitizer with 96 channels sampling at 500 kHz is used to record the data. The resulting Nyquist frequency is 250 kHz, well above the fluctuation frequency. Samples are obtained for a duration of 2 s at each radial location, allowing for low-variance estimation of the fluctuation statistics. The measured data are filtered by a 5–250 kHz band-pass filter before being used in the analysis.

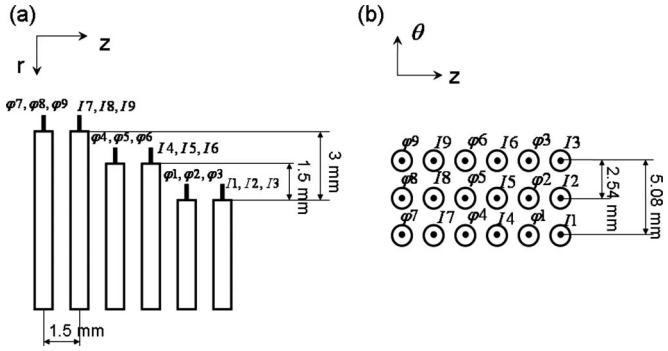

FIG. 1. (a, b) Schematic of the multi-tip (18-tip) probe array.

A Phantom v.7 fast-framing camera is placed at the end of the machine to capture the motion of the plasma visible light emission. The frame rate used here is 100 000/s with 64×64 image resolution, and a Pentax 50 mm $f/1.4$ lens is used in the experiments. Some statistical properties of the turbulent fluctuations can be obtained from the imaging. The Langmuir probe is out of the plasma when recording images.

III. RADIAL PROFILES OF EQUILIBRIUM AND FLUCTUATING QUANTITIES

The fluctuation frequencies are well below the ion cyclotron frequency ($\omega/\Omega_{ci}\sim 0.03-0.3$), and the ion-ion collision frequency is marginally below the ion cyclotron frequency ($V_{ii}/\Omega_{ci}\sim 0.3-1.0$). Thus, it is reasonable to assume that the convecting velocity fluctuations are given by $E\times B$ drift, where the electric field is due to the electrostatic perturbation of the drift turbulence. The radial and azimuthal electric field fluctuations are computed by $\delta E_r=-\Delta\delta\varphi/\Delta x_r$ and $\delta E_\theta=-\Delta\delta\varphi/\Delta x_\theta$, where $\Delta x_\theta=0.5$ cm, $\Delta x_r=0.3$ cm, and $\delta\varphi$ is the fluctuating floating potential. Here we assume the electron temperature fluctuation is negligible. Therefore, from the relation $\varphi_p\cong\varphi+\chi T_e$,[16] where φ_p is plasma potential, φ is floating potential, and T_e is electron temperature, fluctuating plasma potential is approximately equal to the fluctuating

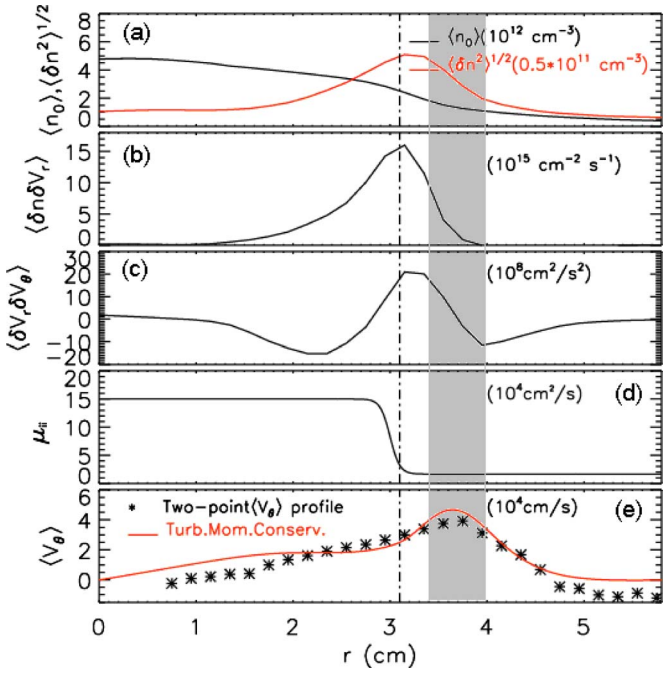

FIG. 2. (Color online) Radial profiles of relevant equilibrium quantities: (a) Time-averaged density profile (black solid line) and RMS amplitudes of density fluctuations (solid red line). (b) Time-averaged turbulent radial particle flux. (c) Time-averaged turbulent Reynolds stress. (d) Model of the ion-ion viscosity profile estimated from measured plasma density and line-averaged ion temperature. (e) Mean azimuthal velocity profiles measured by the two-point technique ("*") and predicted by turbulent ion momentum balance (red solid line). In all figures the dot-dashed line is the position of the density gradient maximum. Shadow region indicates the shear layer location.

floating potential, $\delta\varphi_p \approx \delta\varphi$. We assume the plasma fluid flow is dominated by the $E\times B$ drift; thus, the turbulent Reynolds stress is obtained by $\delta v_r \delta v_\theta = \delta E_r \delta E_\theta / B_0^2$.

Figures 2(a) and 2(b) show the radial profile of time-averaged plasma density and the amplitude of the density fluctuations, as well as the radial particle flux for the plasma condition $B_o = 1$ kG and gas pressure $P = 4$ mTorr. As can be seen the fluctuation amplitude peaks near the region of maximal density gradient; i.e., $r \sim 3.1$ cm. (This position is shown by the dot-dashed line on all the radial profiles in this paper.) Previous work has shown these fluctuations are collisional drift waves.[15] Measurements of the mean azimuthal plasma velocity using the two-point estimation technique, along with the momentum balance analysis,[8] using the model of the ion-ion viscosity profile shown in Fig. 2(d) are also shown in Fig. 2(e). The results show that the plasma exhibits roughly solid body rotation for $r < 3.5$ cm, while for the region $r > 4$ cm the azimuthal velocity is inversely proportional to the radius. A radial shear layer of the azimuthal velocity then exists at the interface region located between 3.5 cm $< r < 4$ cm, which is shown by the shadow region on all the radial profiles in this paper. In previous work we have shown that this shear layer is consistent with the experimentally observed turbulent Reynolds stress for reasonable estimates of the collisional ion-ion viscosity.[8,9] The effects of different ion-ion viscosity profiles are also examined here, and are discussed in Sec. VI.

Figure 2(c) shows the radial profile of the time-averaged Reynolds stress $\langle \delta v_r \delta v_\theta \rangle$. In this paper we use an averaging timescale of 0.45 ms, which corresponds to the timescale needed for the plasma at $r = 3.6$ cm to rotate once in the azimuthal direction (and thus this timescale provides an effective average over all fluctuations with azimuthal mode number $m > 0$). Because CSDX operates in a steady state we record several 10^3 plasma rotation periods resulting in small statistical variance (which is within the thickness of the lines for these results). In this figure the $\langle \delta v_r \delta v_\theta \rangle$ profile peaks at $r \sim 3.3$ cm, while at $r < 2.8$ cm and $r > 3.8$ cm, the Reynolds stress becomes negative. Earlier results show that the divergence of the Reynolds stress (which then indicates either the concentration or diffusion of angular momentum) is balanced by the dissipation profile.[8,9] We notice that the relative shape of the Reynolds stress profile shown in Fig. 2(c) is very similar to our earlier results,[8,9] but that the amplitude of the turbulent Reynolds stress is 2–3 times larger than that shown previously. The origins of this discrepancy are not completely understood, but might be due to the use of a Langmuir probe array in the older work which possibly had more shadowing effects between the probe tips since the ceramic block size was larger than the one used in this paper. But we have not quantified this shadowing effect, so at present, this discrepancy has not been understood completely. However, as we have pointed out, the shape of the Reynolds stress profile is similar.

IV. STATISTICAL PROPERTIES OF REYNOLDS STRESS

In this paper, we are interested in the origin of the shape of the turbulent Reynolds stress profile, since it is this shape that enters most critically into the turbulent momentum conservation equation. We therefore use different statistical analyses tools to investigate the statistical properties of the turbulent Reynolds stress, including calculation of the power spectrum, cross-phase, and cross-coherence between the two fluctuating velocity components, as well as the PDF of the velocities.

The time-averaged Reynolds stress $\langle \delta v_r(t) \delta v_\theta(t) \rangle$ can be computed in frequency space as[17]

$$\langle \delta v_r(t) \delta v_\theta(t) \rangle = C_{\delta v_r \delta v_\theta}(\tau = 0) = \int_{-\infty}^{+\infty} S_{\delta v_r \delta v_\theta}(f) e^{i2\pi f \tau} df|_{\tau=0}, \quad (1)$$

where C is the cross-covariance between $\delta v_r(t)$ and $\delta v_\theta(t)$, τ is the time lag, and $S_{\delta v_r \delta v_\theta}(f)$ is cross-spectrum between $\delta v_r(t)$ and $\delta v_\theta(t)$. Since the co-spectrum $[\mathrm{Re}\, S_{\delta v_r \delta v_\theta}(f)]$ is an even function of f and the quad-spectrum $[\mathrm{Im}\, S_{\delta v_r \delta v_\theta}(f)]$ is an odd function of f, Eq. (1) becomes

$$\langle \delta v_r(t) \delta v_\theta(t) \rangle = 2 \int_0^{+\infty} \mathrm{Re}[S_{\delta v_r \delta v_\theta}(f)] df, \quad (2)$$

and we arrive at

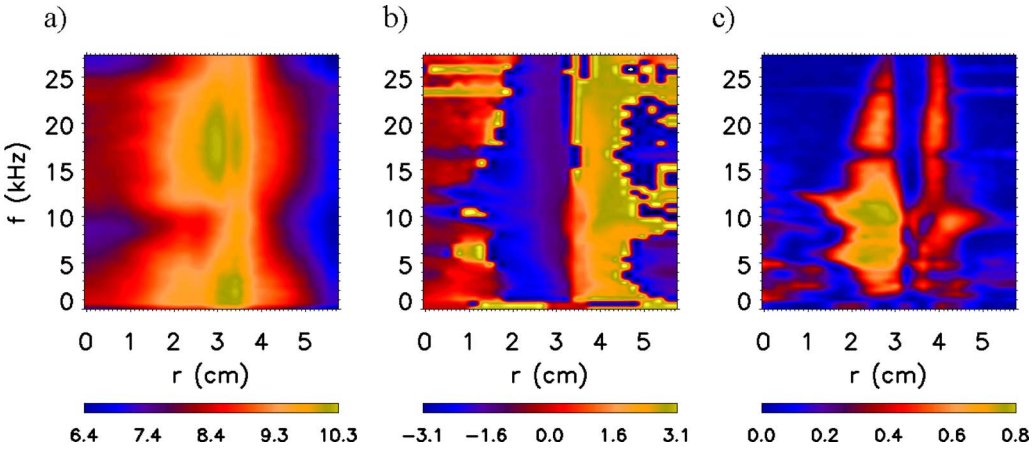

FIG. 3. (Color online) (a) Absolute magnitude of the power spectrum of the turbulent Reynolds stress ($\log_{10}$). (b) Cross-phase between radial and azimuthal turbulent velocity fields $\alpha_{\delta v_r \delta v_\theta}$. (c) Squared cross-coherence between radial and azimuthal turbulent velocity fields $\gamma^2_{\delta v_r \delta v_\theta}$.

$$\langle \delta v_r(t)\, \delta v_\theta(t) \rangle = \int_0^{+\infty} T(f) df, \quad \text{where}$$

$$T(f) = 2\gamma_{\delta v_r \delta v_\theta} \cos \alpha_{\delta v_r \delta v_\theta} \sqrt{S_{\delta v_r \delta v_r}(f)} \sqrt{S_{\delta v_\theta \delta v_\theta}(f)}. \tag{3}$$

This representation allows us to determine how the cross-spectrum $S_{\delta v_r \delta v_\theta}(f)$, cross-phase $\alpha_{\delta v_r \delta v_\theta}$, defined as

$$\alpha_{\delta v_r \delta v_\theta} = \arctan\left[\frac{\mathrm{Im} S_{\delta v_r \delta v_\theta}(f)}{\mathrm{Re} S_{\delta v_r \delta v_\theta}(f)}\right],$$

and the cross-coherence $\gamma_{\delta v_r \delta v_\theta}$, defined as

$$\gamma_{\delta v_r \delta v_\theta} = \sqrt{\frac{|S_{\delta v_r \delta v_\theta}(f)|^2}{S_{\delta v_r \delta v_r}(f) S_{\delta v_\theta \delta v_\theta}(f)}},$$

contribute to the total Reynolds stress.

The absolute magnitude of the frequency-resolved power spectrum $P_{R(t)}(f)$ of the turbulent Reynolds stress $R(t) = \delta v_r(t)\, \delta v_\theta(t)$ at 1 kG is shown in Fig. 3(a). The strongest power featured at 15–23 kHz is located at approximately $r \sim 3.3$ cm, which is close to the region of density gradient maximum. Using our previously published azimuthal wavenumber spectra,[15] these frequencies correspond to azimuthal wave numbers in the range of 2–3 cm^{-1}, which correspond to an azimuthal mode number m=5–10. Thus, the Reynolds stress is driven by fluctuations with spatial scales that are significantly smaller than the plasma column radial scale. Most power of the turbulent Reynolds stress is concentrated in the region from $r \sim 2$ cm to $r \sim 5$ cm with broadband frequency properties. Outside this region the power drops off rapidly. Figures 3(b) and 3(c) show the radial and frequency resolved cross-phase $\alpha_{\delta v_r \delta v_\theta}$ between $\delta v_r(t)$ and $\delta v_\theta(t)$ and the squared cross-coherence $\gamma^2_{\delta v_r \delta v_\theta}$. In both figures we see significant variations in a region from $r \sim 3.0$ cm to $r \sim 3.8$ cm, with cross-phase first changing from $-\pi$ to 0 then to π (or equivalently $-\pi$), and the coherence changing from 0.8 to 0 then back to 0.5. [The sign here is such that a positive cross-phase means $\delta v_r(t)$ leads $\delta v_\theta(t)$ in time.] This region is the same as where the shear flow is located. It is also interesting to note that the innermost location of this phase change coincides with the mean density gradient maximum location and, as shown below, coincides with the birth location of outward-going positive density events. The power-weighted averages over frequency of these two quantities defined as

$$\langle \alpha_{\delta v_r \delta v_\theta} \rangle = \frac{\int \alpha_{\delta v_r \delta v_\theta}(f) |S_{\delta v_r \delta v_\theta}(f)| df}{\int |S_{\delta v_r \delta v_\theta}(f)| df}$$

and

$$\langle \gamma^2_{\delta v_r \delta v_\theta} \rangle = \frac{\int \gamma^2_{\delta v_r \delta v_\theta} |S_{\delta v_r \delta v_\theta}(f)| df}{\int |S_{\delta v_r \delta v_\theta}(f)| df}$$

are shown in Figs. 4(a) and 4(b). It is clear that at $r \sim 3.4$ cm the cross-phase goes to 0, while the coherence drops down to 0.2. The fact that the cross-coherence nearly vanishes at the shear location indicates that there is only a

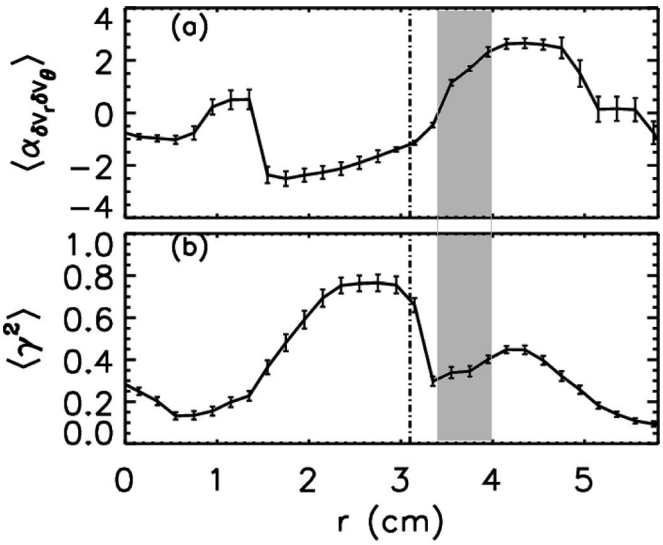

FIG. 4. (a) Power-weighted average cross-phase $\langle \alpha_{\delta v_r \delta v_\theta} \rangle$. (b) Power-weighted average squared cross-coherence $\langle \gamma^2_{\delta v_r \delta v_\theta} \rangle$.

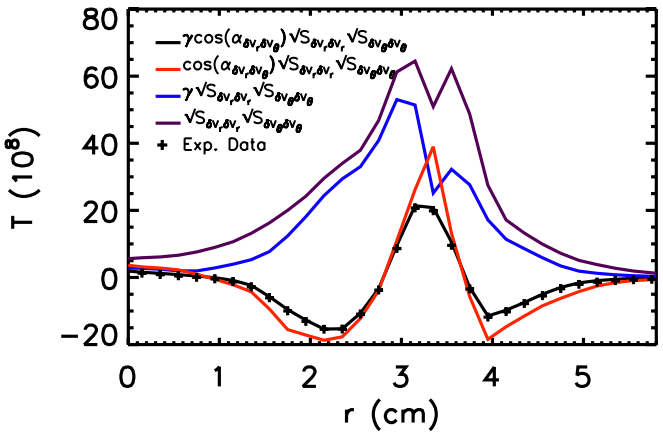

FIG. 5. (Color online) Experimentally measured time-averaged turbulent Reynolds stress (plus sign). Calculation including all factors of power spectrum, cross-phase and cross-coherence (black solid line), calculation with both cross-phase and cross-coherence excluded (purple solid line), calculation with cross-phase only excluded (blue solid line), and calculation with cross-coherence only excluded (red solid line).

weak statistical correlation between the two fluctuation velocity components at this position. As a result, the cross-phase between the two velocity components must vary nearly randomly in the interval $[-\pi, \pi]$ at the shear layer location from one ensemble to the next, as might be expected for two randomly phased signals. When averaged over many statistical ensembles, the cross-phase then averages to a small value at the point where the cross-coherency vanishes.

Figure 5 shows the comparisons between the time-averaged Reynolds stress directly measured in experiments and from the above computations, in which the black solid line includes all the factors of power-spectrum, cross-phase, and cross-coherence, and the blue, red, and purple solid lines exclude the cross-phase, cross-coherence, and both, respectively. It is found that when the cross-phase is excluded, the profile differs significantly from the experimental measurements, which are represented by the "+" symbol. However, when the cross-coherence only is excluded, the profile agrees strikingly well with direct measurements. This shows that the cross-phase provides the dominant contribution to the shape and magnitude of the Reynolds stress. The radial and frequency resolved cosine of the cross-phase is evaluated, as well as the power-weighted average cosine of cross-phase, which is shown in Figs. 6(a) and 6(b). The cosine of the cross-phase changes sign at $r \sim 2.8$ cm and $r \sim 3.8$ cm, which is the same as where the time-averaged Reynolds stress changes sign. This result indicates again that the cross-phase determines the shape of the time-averaged Reynolds stress.

These fast Fourier transform-based analyses provide a time-averaged view of the turbulence. To obtain insight into the dynamics of the turbulence, we now look at the PDF and the skewness (i.e., the third moment of the PDF) of the turbulent Reynolds stress. Figure 7(a) shows the turbulent Reynolds stress PDF at three different radial locations. At $r \sim 2$ cm, which is inside of the shear layer and density gradient maximum, the PDF shows a significant negative skewness [see also Fig. 7(b)] indicating that on average the Reynolds stress is composed of either outward-going transport of negative azimuthal velocity events, or of inward-going positive azimuthal velocity events. At $r \sim 2.8$ cm the PDF is close to symmetric, indicating no preferential transport of azimuthal momentum. At $r \sim 3.4$ cm, which is between the density gradient maximum and shear layer, the Reynolds stress PDF has a large (>1) positive skewness indicative of intermittent or bursty momentum transport events which are characterized by outward-going positive turbulent azimuthal velocities. Figure 7(b) shows the radial profile of the skewness of the turbulent Reynolds stress. A comparison of Fig. 7(b) with Fig. 6(b) shows that the location where the skew-

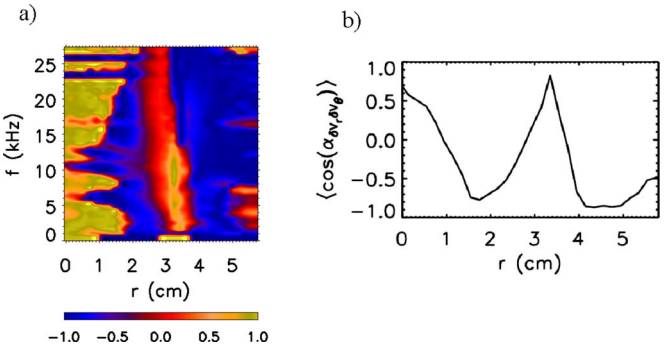

FIG. 6. (Color online) (a) Radial and frequency resolved $\cos(\alpha_{\delta v_r \delta v_\theta})$, and (b) power-weighted average $\langle \cos(\alpha_{\delta v_r \delta v_\theta}) \rangle$.

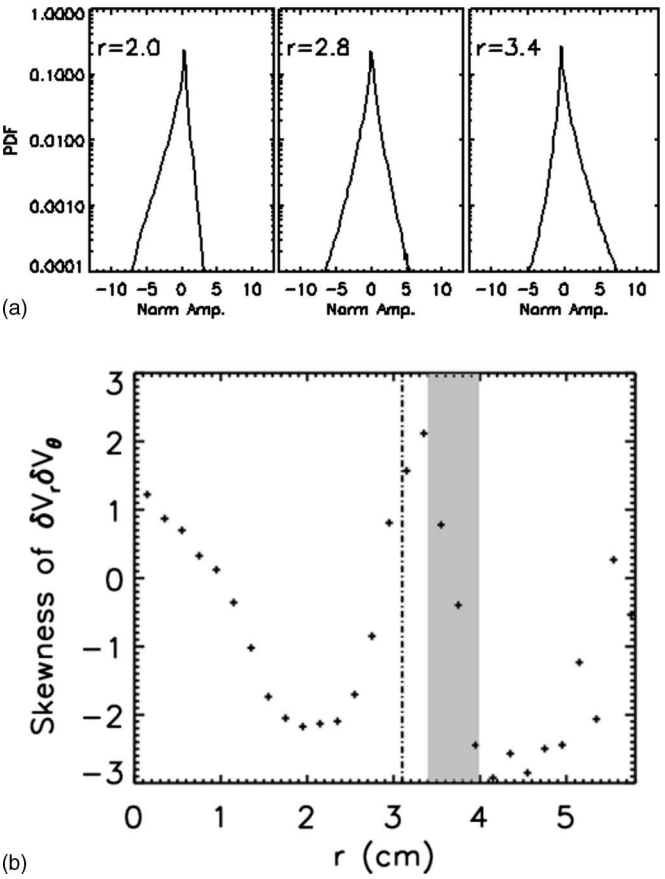

FIG. 7. (a) Turbulent Reynolds stress PDF at three radial locations (normalized by standard deviation), and (b) radial profile of the skewness of the turbulent Reynolds stress $\delta v_r \delta v_\theta$.

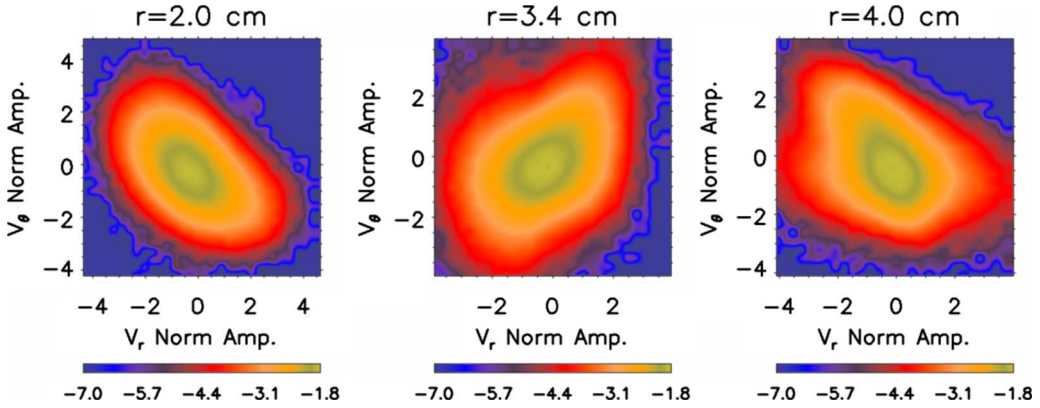

FIG. 8. (Color online) Joint PDF of radial and azimuthal velocity fields at three radial locations ($\log_{10}$). Normalization is standard deviation.

ness of the turbulent Reynolds stress is significantly positive (i.e., where outward-going bursts of positive plasma flow occur) is linked to the variation of the cosine of the cross-phase between the radial and azimuthal turbulent velocity fields. This is borne out by an examination of the joint PDF of the turbulent velocity fluctuations seen in Fig. 8. At $r\sim 2$ cm and $r\sim 4$ cm, the PDFs are oriented from the second quadrant pointing down towards the fourth quadrant, consistent with radial velocities that are out of phase with the azimuthal velocities. At $r\sim 3.4$ cm, the velocities are in phase, and thus the joint PDF is oriented along an axis running from the first quadrant to the third quadrant.

V. RELATIONSHIP BETWEEN INTERMITTENT DENSITY FLUCTUATIONS AND REYNOLDS STRESS

It has been reported that there is a universal nature to bursts of outward-going blobs of plasma in the edge of magnetic confinement laboratory plasma devices such as tokamaks[18] and stellarators.[19] These blobs have also been referred to as intermittent plasma objects in the literature.[18] One simple signature of such events is that the PDF of the ion-saturation current exhibits strongly non-Gaussian distributions in regions where these events are being generated and propagating. Several mechanisms of the generation of these intermittent turbulent structures have been reported.[20,21] These earlier results, and the behaviors of the Reynolds stress PDF discussed above, motivate us to examine the PDF of the ion-saturation current. Here we provide experimental results which suggest that the behavior of the turbulent Reynolds stress and the generation of intermittent density bursts at the region are all related. Such a link may show the causality, or it is also possible that it may simply show the modification of the statistical properties of the fluctuations in the vicinity of the shear flow.

Figure 9(a) shows the PDF of ion-saturation current at three different radial locations: $r=2$ cm, $r=2.8$ cm, and $r=3.4$ cm. At $r=2$ cm the ion-saturation fluctuation is skewed negatively, indicating a predominance of negative going density events, while at $r=3.4$ cm, the fluctuation is skewed positively, indicating a predominance of positive going density events at this location. At $r=2.8$ cm the distribution is close to symmetric, indicating that the outward-going (inward-going) positive (negative) density events are generated near the maximum density gradient. The Isat PDF behavior shown in Fig. 9 is also similar to those observed in the linear device LAPD[22] as well as at the edge of tokamak plasma devices.[18] Figure 9(b) shows the radial profile of the skewness of ion-saturation current fluctuations computed from the Isat PDF at each radial location. The Isat skewness changes sign at $r\sim 2.7$ cm, and reaches a maximum near $r\sim 4$ cm, after which it decays at larger radii. This behavior is consistent with the generation of positive bursts of density near the density gradient maximum.

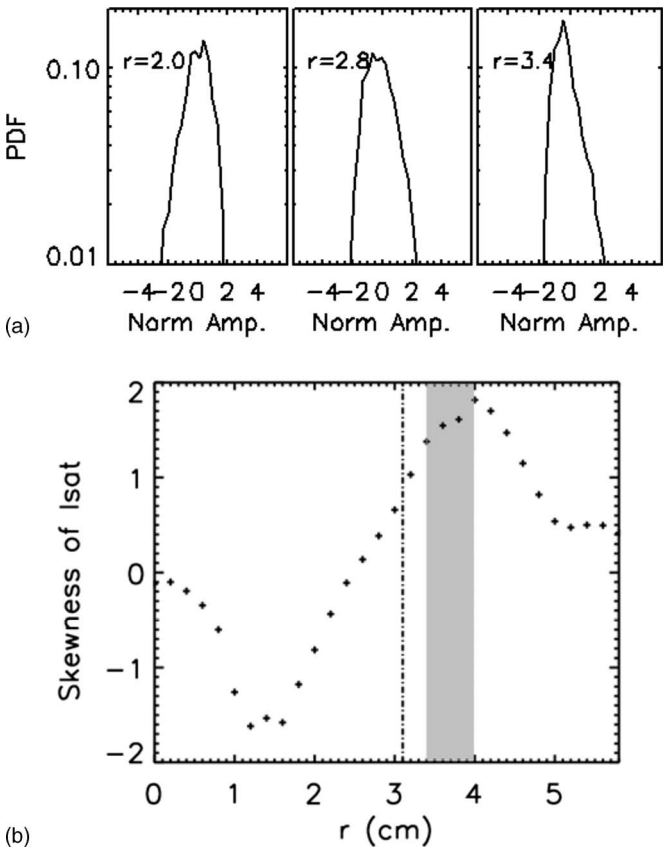

FIG. 9. (a) PDF of the fluctuating ion-saturation current at three radial locations (normalized by standard deviation), and (b) radial profile of the skewness of the fluctuating ion-saturation current.

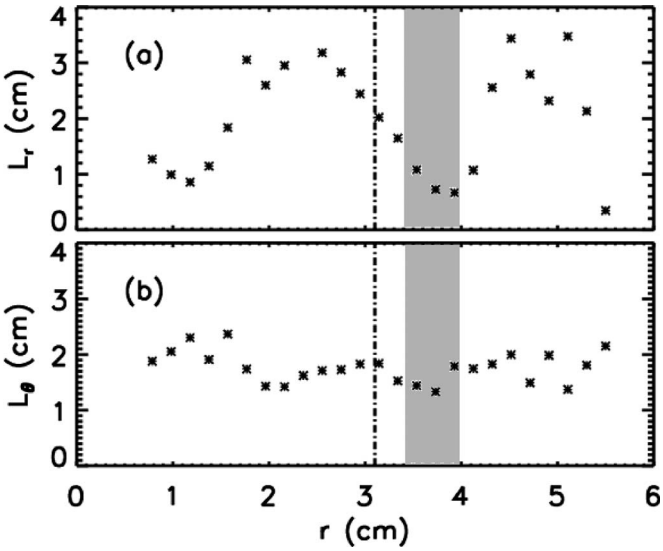

FIG. 10. (a) Radial turbulence correlation length and (b) azimuthal turbulence correlation length, both estimated from fast-imaging.

We can gain additional insight by examining the radial and azimuthal turbulence correlation lengths computed from fast-framing imaging data (Fig. 10). These correlation lengths are obtained by computing the cross-correlations between the fluctuating intensity at two radially or azimuthally separated positions. The cross-correlation function envelope is then used to find the correlation length, defined as the location where the envelope is down by a factor of $1/e$ from the peak value at zero spatial separation. The light intensity of the image is somewhat correlated to the density fields, but also likely is influenced by the electron temperature fluctuations and neutral density. Regardless of this fact, we can still gain insight into the turbulence dynamics from this analysis. On the core side of the density gradient maximum the radial correlation length is larger than the azimuthal correlation length. Near the shear layer, there is a pronounced dip in the radial turbulence correlation length which is reduced to a few millimeters ($\sim$3 mm) at the location of maximum flow shear, while the azimuthal turbulence correlation length is unchanged (1.5–2 cm). These results, with the Isat PDF shown above, indicate that the density fluctuations originate at or near the density gradient maximum and have, on average, a radially elongated shape at this location. Near the shear layer these turbulent fluctuations are elongated in the azimuthal direction, with an azimuthal correlation length that is about 3–4 times larger than the radial correlation length. This behavior is similar to the $E \times B$ flow shear decorrelation process that is thought to occur in the edge of H-mode tokamak plasmas.[23] Outside the shear layer these perturbations recover their radially elongated shape, and move on average away from the shear layer. This is consistent with the observation of fingerlike blobs near 4–5 cm from imaging in previous studies.[24]

The joint PDF of the turbulent radial particle flux and the Reynolds stress is also investigated, as seen in Fig. 11. At $r \sim 2$ cm and $r \sim 4$ cm, these PDFs are oriented from second quadrant to the fourth quadrant, and the largest probabilities lie in the second quadrant, indicating that the momentum transport is associated with outward-going particle flux carrying a deficit of azimuthal momentum (i.e., a negative momentum fluctuation), which is consistent with negative skewness of the turbulent Reynolds stress at those locations. At $r \sim 3.4$ cm, the joint PDF is oriented from the first quadrant to the third quadrant, with the largest probability lying in the first quadrant. This suggests that near the shear layer the bursty momentum transport is associated with outward-going particle flux fluctuations carrying an excess of azimuthal momentum (a positive momentum fluctuation), consistent with the positive skewness of the turbulent Reynolds stress. An empirical investigation between the momentum and the particle transport was reported in the boundary region of fusion plasmas and suggested the same conclusion.[25] In the time-averaged analysis above, the cross-phase was shown to determine the detailed shape of the time-averaged Reynolds stress profile, which in turn is linked to the time-averaged velocity shear layer. The Reynolds stress measurements, ion-saturation current PDF, and the joint PDF between Reynolds stress and radial particle flux suggest that the turbulent Reynolds stress is associated with radially directed plasma density events, which also carry azimuthal plasma flow and momentum. A significant negative radial divergence to such bursts of angular momentum transport will then lead to the concentration of azimuthal flow in that region.[26]

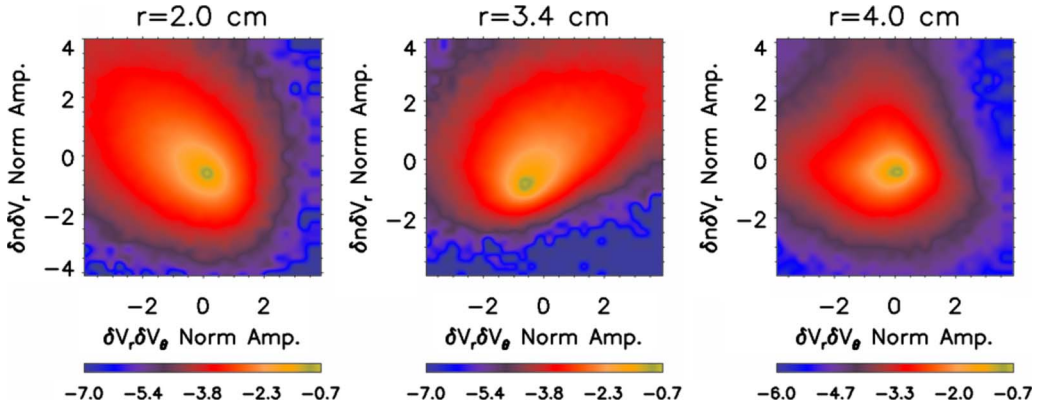

FIG. 11. (Color online) Joint PDF of radial particle flux and the turbulent Reynolds stress at three radial locations ($\log_{10}$). Normalization is standard deviation.

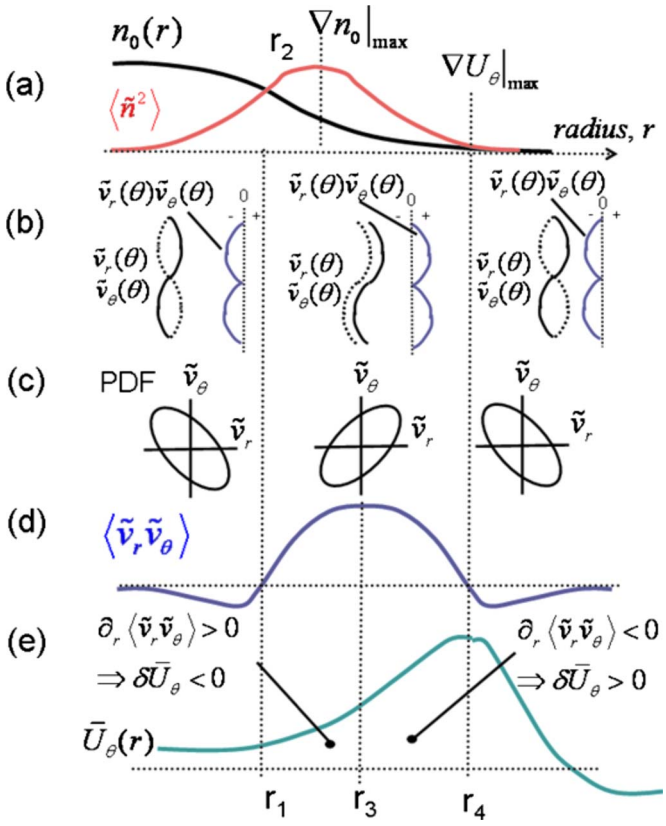

FIG. 12. (Color online) Physical picture of shear flow generation from drift turbulence.

VI. DISCUSSION

The above results suggest a physical picture of shear flow generation shown in Fig. 12. The density fluctuations, due to collisional drift waves, have a peak amplitude at the largest density gradient region located at $r \sim r_2$ [Fig. 12(a)]. The Isat skewness results show that at or near this region the outgoing density bursts or blobs are generated and on average form outward-going positive density excursions, resulting in a positive Isat skewness at r_2. For $r < r_1$, these perturbations carry angular momentum with fluctuating radial and azimuthal velocity fields that are out of phase [Fig. 12(b)], resulting a velocity PDF, as shown in Fig. 12(c). As a result, the mean Reynolds stress is negative in the region $r < r_1$. In the region $r > r_2$, on average the fluctuations consist of outward-going positive density events which have a positive azimuthal velocity increment associated with them. Thus, in the region $r_2 < r < r_4$ the fluctuating radial and azimuthal velocity fields are in phase resulting in a positive mean Reynolds stress in this region [Fig. 12(b)]. The joint velocity PDF then has the orientation shown in Fig. 12(c). The location of the positive Isat skewness coincides with the positive turbulent Reynolds stress skewness, suggesting that the bursts of positive stress are associated with bursts of density, consistent with the results shown in Fig. 11. The mean Reynolds stress decays for $r > r_3$ since the background density gradient is weaker here and thus the turbulence drive is weaker. In addition, the Reynolds stress couples energy from the higher frequency fluctuation scales into the shear flow, resulting in a decrease in fluctuation amplitude in this region. As a result, there is a peak in the turbulent stress located at $r \sim r_3$, which lies between the density gradient maximum and the shear layer located at r_4. The divergence of the Reynolds stress thus changes sign across the region from r_1 to r_4. A negative radial divergence to the momentum flux will act to amplify a positive azimuthal flow, resulting in the formation of a positive going flow in the region $r_3 < r < r_4$; a positive radial divergence to the momentum flux will drive a negative mean azimuthal flow, so the plasma rotation could be reversed either for $r_1 < r < r_3$ or for $r > r_4$. Evidence for such a flow reversal at large radius is indeed seen in our data [see Fig 2(e)]. However, we expect that the collisional ion-ion viscosity is largest near $r \sim 0$ (Refs. 8 and 9) and it will act to dissipate the shear flow in the central part of the plasma column, resulting in nearly solid body rotation in this portion of the plasma. A detailed study of the effect of the ion-ion viscosity on plasma rotation is discussed below.

Theory predicts that, since the turbulence shear flow interaction conserves energy, the radial correlation length of the turbulence will decrease,[3] as seen in our observations. The reduction in radial correlation length is most pronounced where the Reynolds stress changes sign at r_4. At this location there is little or no radial transport of azimuthal momentum even though there are finite velocity fluctuations. Thus, either the cosine of the velocity cross-phase and/or cross-coherency of the two velocity components must vanish at this point. The link between the PDFs of the Isat, Reynolds stress and the joint PDF of particle flux and Reynolds stress suggests a hypothesis where the plasma density fluctuations born near the maximum density gradient also carry angular momentum as well, and thus may in fact be two elements of the same underlying phenomena. Taken together with recent results from the TORPEX device[27] which show that the density blobs are formed by flow-shear "pinching-off" drift-interchange fingers of plasma extending from a dense core region into a lower density scrape-off layer region, these results point towards a strong link between turbulent generated shear layer formation, shear layer mediated bursty transport, angular momentum transport, and spontaneous central plasma column rotation. We are now planning experiments to test this picture using a combination of probe-based and fast imaging based diagnostics, and will report the results in future publications.

In the initial ion momentum balance analysis presented in Refs. 8 and 9, we assumed a steplike model of the ion-ion viscosity $\mu_{ii} = \rho_i^2 \nu_{ii} \propto n T_i^{-1/2}$ since we did not measure a radial profile of T_i. Here, we perform an analysis with different μ_{ii} profiles to better understand its effect on shear flow generation. Figure 13(a) is μ_{ii} with different radial profiles (steplike model and Gaussian, consistent with the mean density and ion temperature decreasing with r, since $\mu_{ii} \propto n T_i^{-1/2}$), and (b) is the mean azimuthal velocity field computed from ion momentum balance equation with assumed μ_{ii} profiles in (a). The colors in the two figures correspond. The symbols "*" are the experimental measurements of the azimuthal velocity. In both figures, the black dashed lines indicate the largest positive radial divergence to the angular momentum flux and the red dashed lines indicate the largest negative radial di-

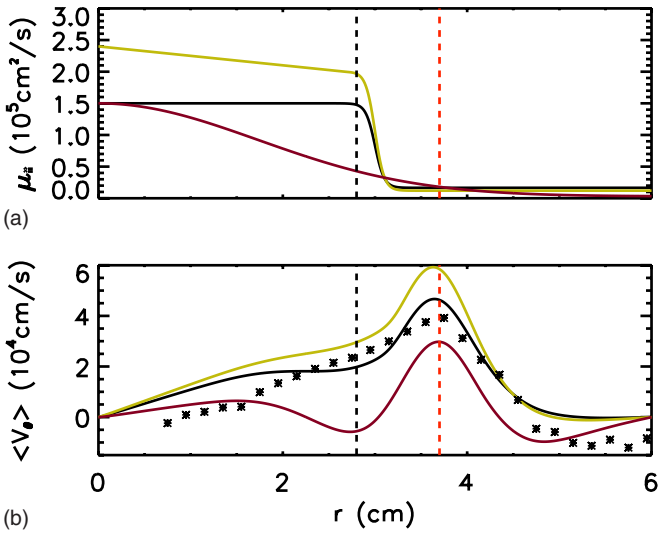

FIG. 13. (Color online) (a) Assumed ion-ion viscosity profiles and (b) mean azimuthal velocity from ion momentum balance analysis.

vergence to the angular momentum flux. It shows that when the ion-ion viscosity is large enough at the location of the largest positive radial divergence to the momentum flux, the ion-ion viscosity drag transfers the azimuthal flow at the shear layer to the central part of the plasma column and generates nearly solid body rotation inside the shear layer. If the ion-ion viscosity is small, then the plasma rotation could be reversed due to the effect of the Reynolds stress. Similar results are also found in the numerical simulations.[28] With a proper radial profile of μ_{ii}, the mean azimuthal velocity computed from the momentum balance equation will match the experimental results, as we have shown in Fig. 2. Further refinements to this investigation will be carried out in the future by retaining a more complex form of the viscous stress tensor which includes the higher-order ν_{ii}/Ω_{ci} terms neglected here,[29] and including the radial variation of the viscosity coefficient when calculating the divergence of the stress tensor.

VII. SUMMARY

In summary, we have directly measured the Reynolds stress using Langmuir probes in a linear machine and analyzed the data statistically. We found the cross-phase between radial and azimuthal velocity fluctuations is the key factor to determine the shape and the amplitude of the Reynolds stress. The skewness of turbulent Reynolds stress shows a positive peak at $r \sim 3.4$ cm, and coincides with positively skewed Isat events. The observations indicate a link between the behavior of the Reynolds stress, its cross-phase and cross-coherence, generation of bursty radially going density and azimuthal momentum transport events, and the formation of the large-scale shear layer. Ideally one would like to see the dynamical coupling between the azimuthal momentum transport and the particle transport. We are planning this in our future experiments.

ACKNOWLEDGMENTS

This research was performed under U.S. Department of Energy (DOE) Grant No. DE-FG02-06ER54871.

[1] W. Horton, Rev. Mod. Phys. **71**, 735 (1999).
[2] C. Hidalgo, Plasma Phys. Controlled Fusion **37**, A53 (1995).
[3] H. Diamond, S.-I. Itoh, K. Itoh, and T. S. Hahm, Plasma Phys. Controlled Fusion **47**, R35 (2005).
[4] M. Jakubowski, R. J. Fonck, and G. R. McKee, Phys. Rev. Lett. **89**, 265003 (2002).
[5] G. D. Conway, B. Scott, J. Schirmer, M. Reich, A. Kendl, and the ASDEX Upgrade Team, Plasma Phys. Controlled Fusion **47**, 1165 (2005).
[6] Y. H. Xu, C. X. Yu, J. R. Luo, J. S. Mao, B. H. Liu, J. G. Li, B. N. Wan, and Y. X. Wan, Phys. Rev. Lett. **84**, 3867 (2000).
[7] A. Fujisawa, K. Itoh, H. Iguchi, K. Matsuoka, S. Okamura, A. Shimizu, T. Minami, Y. Yoshimura, K. Nagaoka, C. Takahashi, M. Kojima, H. Nakano, S. Ohsima, S. Nishimura, M. Isobe, C. Suzuki, T. Akiyama, K. Ida, K. Toi, S.-I. Itoh, and P. H. Diamond, Phys. Rev. Lett. **93**, 165002 (2004).
[8] C. Holland, J. H. Yu, A. James, D. Nishijima, M. Shimada, N. Taheri, and G. R. Tynan, Phys. Rev. Lett. **96**, 195002 (2006).
[9] G. R. Tynan, C. Holland, J. H. Yu, A. James, D. Nishijima, M. Shimada, and N. Taheri, Plasma Phys. Controlled Fusion **48**, S51 (2006).
[10] C. Hidalgo, C. Silva, M. A. Pedrosa, E. Sanchez, H. Fernandes, and C. A. F. Varandas, Phys. Rev. Lett. **83**, 2203 (1999).
[11] V. Antoni, E. Spada, N. Vianello, M. Spolaore, R. Cavazzana, G. Serianni, and E. Martines, Plasma Phys. Controlled Fusion **47**, B13 (2005).
[12] G. S. Xu, B. N. Wan, and J. Li, 20th IAEA Fusion Energy Conf., Vilamoura, Portugal, 2004, IAEA-CN-116/EX/8/-4Rb.
[13] P. H. Diamond and Y.-B. Kim, Phys. Fluids B **3**, 1626 (1991).
[14] G. R. Tynan, A. D. Bailey III, G. A. Campbell, R. Charaton, A. de Chambrier, G. Gibson, D. J. Hemker, K. Jones, A. Kuthi, C. Lee, T. Shoji, and M. Wilcoxson, J. Vac. Sci. Technol. A **15**, 2885 (1997).
[15] M. J. Burin, G. R. Tynan, G. Y. Antar, N. A. Crocker, and C. Holland, Phys. Plasmas **12**, 052320 (2005).
[16] I. H. Hutchinson, *Principles of Plasma Diagnostics* (Cambridge University Press, Cambridge, 1987).
[17] E. J. Powers, J. Y. Hong, and C. P. Ritz, "Applied Digital Time Series Analysis" (Preliminary Version), copyright 1986 by E. J. Powers.
[18] J. Boedo, D. Rudakov, R. Moyer, S. Krasheninnikov, D. Whyte, G. McKee, G. Tynan, M. Schaffer, P. Stangeby, P. West, S. Allen, T. Evans, R. Fonck, E. Hollmann, A. Leonard, A. Mahdavi, G. Porter, M. Tillack, and G. Antar, Phys. Plasmas **8**, 4826 (2001).
[19] R. Sanchez, B. Ph. van Milligen, D. E. Newman, and B. A. Carreras., Phys. Rev. Lett. **90**, 185005 (2003).
[20] P. Diamond and T. S. Hahm, Phys. Plasmas **2**, 3640 (1995).
[21] A. Smolyakov, P. H. Diamond, and M. Malkov, Phys. Rev. Lett. **84**, 491 (2000).
[22] T. A. Carter, Phys. Plasmas **13**, 010701 (2006).
[23] H. Biglari, P. H. Diamond, and P. W. Terry, Phys. Fluids B **2**, 1 (1990).
[24] G. Y. Antar, J. H. Yu, and G. Tynan, Phys. Plasmas **14**, 022301 (2007).
[25] C. Hidalgo, B. Gonçalves, C. Silva, M. A. Pedrosa, K. Erents, M. Hron, and G. F. Matthews, Phys. Rev. Lett. **91**, 065001 (2003).
[26] E. Kim and P. H. Diamond, Phys. Rev. Lett. **88**, 225002 (2002).
[27] S. H. Muller, A. Diallo, A. Fasoli, I. Furno, B. Labit, and M. Podestà, Phys. Plasmas **14**, 110704 (2007).
[28] J. R. Myra, D. A. Russell, and D. A. D'Ippolito, Phys. Plasmas **15**, 032304 (2008).
[29] S. I. Braginskii, *Reviews of Plasma Physics*, edited by M. A. Leontovich (Consultants Bureau, New York, 1965), Vol. 1.